Analyzing coastal erosion and sedimentation using Sentinel-1 SAR change detection
An application on the Volta Delta, Ghana

Di Biase, Valeria; Hanssen, Ramon F.

Research Paper

Analyzing coastal erosion and sedimentation using Sentinel-1 SAR change detection: An application on the Volta Delta, Ghana

Valeria Di Biase [a,*], Ramon F. Hanssen [b]

[a] *Institute for Marine and Atmospheric Research, Department of Physics, Utrecht University, 3584 CC, Utrecht, The Netherlands*
[b] *Department of Geoscience and Remote Sensing, Delft University of Technology, 2628 CN, Delft, The Netherlands*

ARTICLE INFO

ABSTRACT

Ghana's coastline has been facing erosion and sedimentation phenomena for several decades, resulting in a serious threat to life and property considering that major urban settlements are located on the coast. In this region, there has been a lack of emphasis on comprehensive, large-scale investigations into coastal changes: prior research has predominantly centered on site-specific assessments. These studies have revealed alarming erosion rates, with reports indicating that nearly ten meters are lost annually. The use of high-resolution remotely sensed data can be a consistent support in regions where physical or economic obstacles interfere with collecting in situ information. In particular, the use of continuous all-weather SAR data may facilitate the evaluation of erosion and sedimentation phenomena in coastal areas. In this paper, we apply SAR data over a time period between 2017 and 2021. Sentinel-1 data are pre-processed using the Google Earth Engine platform, and a dedicated algorithm is then applied to identify and quantify erosion and sedimentation processes. Optical images are used as a reference for detecting the location of two areas where consistent sedimentation and erosion phenomena occurred in the considered four years. The results demonstrate that SAR backscattering variations over time offer a reliable method for monitoring coastal changes. This approach enables the identification of the type of phenomena occurring - sedimentation or erosion -, and allows for the quantification of their intensity and dimensions over time. The method can be worldwide applied once the appropriate thresholds are evaluated and help in predictive studies and environmental planning.

1. Introduction

Coastal environments are subject to continuous and dynamic changes driven by various natural and anthropogenic factors. The shoreline, defined as the position of the land-water interface at a specific moment in time (Gens, 2010), plays a critical role in coastal ecosystems and human activities. Its continuous displacement, commonly referred to as coastal erosion (Natesan et al., 2015), can have significant environmental and socioeconomic implications. Understanding and quantifying coastal erosion is essential for effective coastal management and sustainable development and these methods benefit natural resource managers, planners, coastal property owners, and scientists (Wang and Allen, 2008). One of the approaches to monitor and quantify coastal erosion is by analyzing changes in littoral profiles (Kana, 2003). Remote sensing techniques have proven invaluable in this endeavor, providing data to enhance our understanding of shoreline dynamics (Rahman et al., 2009; Sepuru and Dube, 2018; Nikolakopoulos et al.,

2019; Apostolopoulos and Nikolakopoulos, 2021). However, coastal environments' dynamic nature, controlled by multiple factors (Pethick, 1984), poses challenges in obtaining accurate and reliable information. Passive remote sensing techniques, such as infrared and short-wave infrared bands, are useful but often limited by weather conditions and atmospheric corrections (Zribi et al., 1997; Elhag et al., 2011; Dong et al., 2014; Elhag and Bahrawi, 2017). As a result, radar-based remote sensing, particularly Synthetic Aperture Radar (SAR), has gained prominence due to its all-weather capabilities and higher reliability; moreover, radar images from certain missions are freely accessible and the role of active remote sensing data in natural resources management is now more comprehensive (Baghdadi et al., 2002; Vrieling, 2006; Schoepfer et al., 2017; Ngo et al., 2020; Sharma et al., 2021). SAR data are well-suited for studying coastal phenomena due to their sensitivity to topography, surface roughness, and moisture content — critical drivers of coastal variability (Di Biase and Hanssen, 2021; Di Biase et al., 2022); they provide valuable information by directly characteriz-

---

* Corresponding author.
  E-mail addresses: v.dibiase@uu.nl (V. Di Biase), r.f.hanssen@tudelft.nl (R.F. Hanssen).
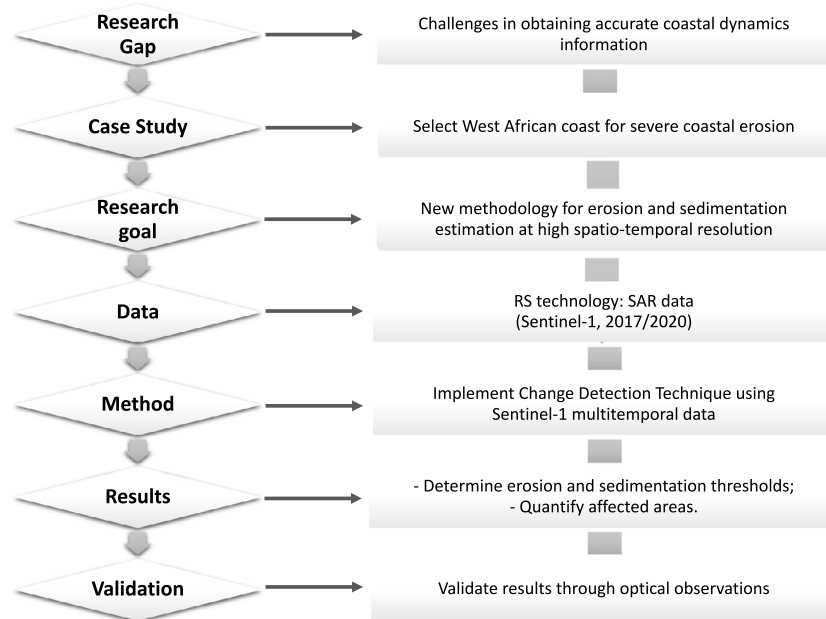
Fig. 1. Graphical index of the paper.

ing surface reflectivity, making it an ideal choice for shoreline change detection (Hachemi et al., 2020). SAR imagery has been extensively applied to various coastal studies, including flood mapping (Horritt et al., 2001; Martinis and Twele, 2010; Pandey et al., 2022), coastal boundary changes (Vrieling, 2006; Zhu et al., 2021), and coastal feature evolution (Hachemi et al., 2015; Vandebroek et al., 2017).

In this research, we focus on the use of SAR data to quantify and identify erosion and sedimentation areas along the eastern coast of Ghana, an area highly susceptible to erosion processes (Wellens-Mensah et al., 2002; Ankrah et al., 2023). The West African coast, including Ghana, faces severe challenges related to coastal erosion, yet comprehensive investigations into shoreline dynamics have been limited (Alves et al., 2020; Ankrah et al., 2023). Previous studies have often concentrated on specific sites or lacked extensive assessments (Wellens-Mensah et al., 2002; Boateng, 2012; Jayson-Quashigah et al., 2019; Appeaning Addo et al., 2020; Alves et al., 2020). Landsat images have been employed to assess shoreline changes along the eastern coast of Ghana on a large spatial scale (Lamptey et al., 2022; Puplampu et al., 2023).

The primary scope of the present work is to present a novel methodology for identifying and quantifying erosion and accretion zones, by leveraging the potential of SAR data from Sentinel-1 satellites. These satellites, renowned for their high spatiotemporal resolution and all-weather capabilities in the C-band (Choi and Hur, 2012), operate at a large spatio-temporal scale, making them the ideal data source to address the current gap in investigating the Ghanaian coastline.

This research introduces an innovative approach grounded in change detection techniques, using multi-temporal SAR data pre-processed through Google Earth Engine (GEE). By discerning subtle variations in backscattering properties along the coastal areas, we aim to demonstrate the feasibility of using SAR data for large-scale evaluations of sedimentation and erosion patterns within the Volta Delta region of Ghana. The presented methodology is not restricted to this specific study case; it can be adapted for extensive inquiries in diverse scenarios, offering the flexibility to fine-tune thresholds and align with various research objectives. In the following sections, we detail the materials (Sect. 2), method (Sect. 3), and results (Sect. 4), providing a comprehensive assessment of coastal erosion dynamics in the Volta Delta region, Ghana. A graphical index of the paper is provided by the flowchart in Fig. 1.

2. Materials

2.1. Study area

Ghana's coastal zone comprises approximately 6.5% of the country's total land area (Armah, 1991). The coastline, spanning 540 Km, is divided into three sections—western, central, and eastern—based on geomorphologic characteristics, as illustrated in Fig. 2 (Ly, 1980). The western section features a flat terrain with expansive beaches and lagoons, characterized by low energy (Alves et al., 2020). In contrast, the eastern part is sandy, hosting barrier lagoons and spits (Angnuureng et al., 2013). The central portion exhibits moderate energy levels, featuring rocky headlands, sandbars, spits, and lagoons (Alves et al., 2020; Angnuureng et al., 2020).
Coastal erosion poses a significant challenge along Ghana's coastline. According to Armah and Amlalo (1998), erosion is not restricted to specific coastal divisions but affects the entire Ghanaian coastline to varying extents. Appeaning Addo et al. (2020) reported an average erosion rate of 1.94 m/year along the eastern shoreline and 0.58 m/year along the western shoreline of the Volta River estuary in Ghana. Boye and Fiadonu (2020) highlighted that, in the western region, some shoreline areas are accreting, while most rocky shorelines are experiencing erosion at varying rates. In coastal Dzita, Ghana, Brempong et al. (2021) found evidence of erosion dominance, with rates of -7.23 ± 0.23 m/year and -4.85 ± 0.23 m/year between May and December 2018 and June and December 2019, respectively.
This study focuses specifically on the central coast, covering a 296 km embayed stretch from the west of Prampram to Cape Three Points, which encloses coastal lagoons (Addo et al., 2018). Addo et al. (2018) documented high rates of erosion and tidal flooding in this area, resulting in the destruction of houses and property.

2.2. Remote sensing data

Sentinel-1 acquires C-band Synthetic Aperture Radar (SAR) data with various polarizations and resolutions. The freely accessible Sentinel-1 data in Google Earth Engine (GEE) is available in Level-1 Ground Range Detected (GRD) format. GRD represents focused SAR data that has undergone detection, multi-looking, and projection to ground range using an Earth ellipsoid model (Di Biase et al., 2022).
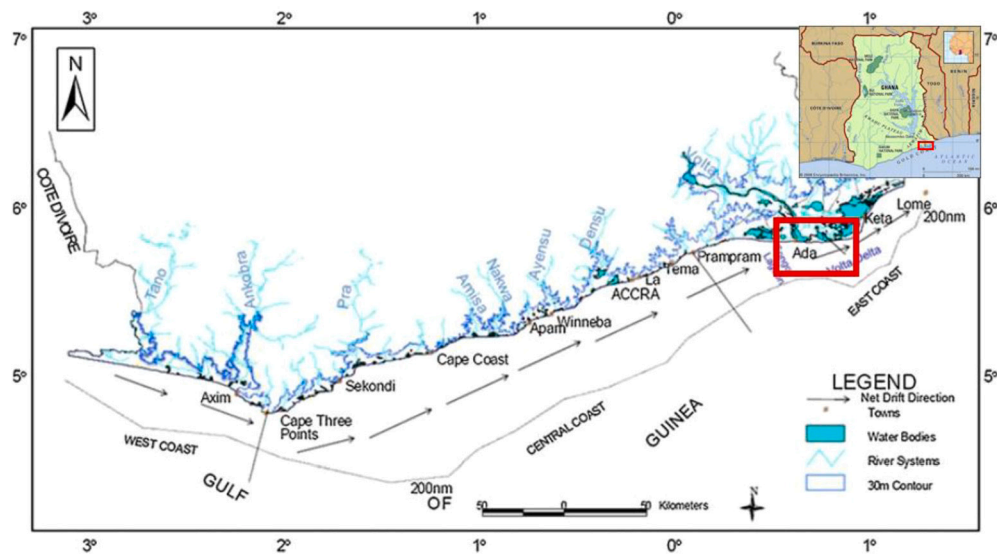
Fig. 2. Drainage, longshore drift and divisions of Ghana's coastline (figure source: Boateng (2012)). In red, the location of the study area.

In the current study, the Interferometric Wide (IW) mode is employed. The spatial resolution is 20 m × 20 m, encompassing 20 m in range (across-track) and 20 m in azimuth (along-track). Both polarizations, VV and VH, are considered.

The preprocessing of the images involves the use of the European Space Agency's (ESA) Sentinel-1 Toolbox (S1TBX), accessible at http://step.esa.int/main/doc/tutorials/, with a more comprehensive description provided by Di Biase et al. (2022). Subsequent steps in the analysis are performed utilizing dedicated algorithms, as illustrated in Fig. 3:

1. Normalization of the backscatter coefficients (Gulácsi and Kovács, 2020): a cosine correction has been performed, which is the most widely used incidence angle correction technique (Ulaby et al., 1982).

2. Speckle filtering: The refined Lee filter (Lee, 1980, 1981), was employed in this study. SAR images are commonly affected by speckle noise, originating from the interference of transmitted and received microwaves at the radar antenna, introduces multiplicative noise that degrades the overall quality of SAR images (Goodman, 1976; Lee, 1986). However, while speckle filtering techniques effectively reduce noise, they often come at the cost of decreased spatial resolution in the filtered SAR images (Pelich et al., 2020). To address this challenge and ensure the preservation of sufficient spatial details, various filtering techniques - as the Lee filter used in this study - can be applied to obtain the desired tradeoff between the signal-to-noise ratio and detail preservation (Bovolo and Bruzzone, 2007).

3. Temporal filtering: a multitemporal filter has been applied to 8-image stacks, spanning a 48-day period, in order to reduce noise and short-term effects (tidal conditions, wind). The applied temporal filter (as in Quegan et al. (2000)), facilitates the reduction of speckle by calculating the combined estimate from several images through averaging. The filter has been applied to the single-polarization SAR stacks. The stack is provided and returned in dB.

2.3. Google Earth imagery

Since its inception in 2005, Google Earth has played an increasingly prominent role in geomorphological research, offering new possibilities for studying landforms and natural processes (Boardman, 2016). Google Earth imagery demonstrates the potential to enhance the geographical context of research and contribute to classificatory and empirical studies (French and Burningham, 2009). Numerous studies use
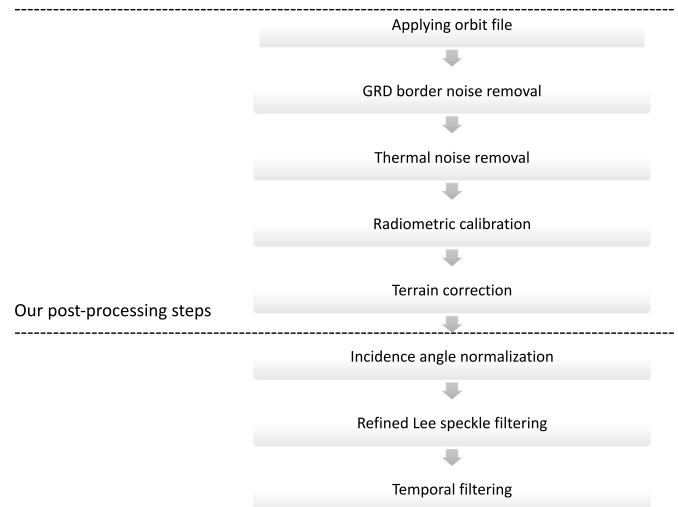

Fig. 3. Flowchart of the data processing steps applied to Sentinel-1 data. Pre-processing steps are performed in GEE, and further steps are performed with dedicated algorithm.

its capabilities; Google Earth has been employed to investigate various geomorphological phenomena, such as river networks (Hackney and Carling, 2011), landslides (Borrelli et al., 2015), coastal features (Pilkey et al., 2009), and soil erosion (Boardman et al., 2015; Boardman, 2016). In this study, we use the Google Earth database, which contains historical remotely sensed data, to serve as a visual reference for identifying areas characterized by consistent erosion and sedimentation in our chosen study area. Our analysis focuses on two key reference points: 2017 and 2022, aligning with the commencement and conclusion of the Sentinel-1 image data used in our methodology. In Fig. 4, the main panel presents a close-up view of the Volta Delta river, offering a detailed perspective on two specific regions. These regions highlight the progression of erosion and sedimentation phenomena from 2017 to 2022, as demonstrated in the accompanying lateral panel. These panels provide an enhanced focus on the areas affected by sedimentation and erosion: the area within the red circle corresponds to the erosion zone, while the area enclosed by the green circle indicates the sedimentation-affected area.
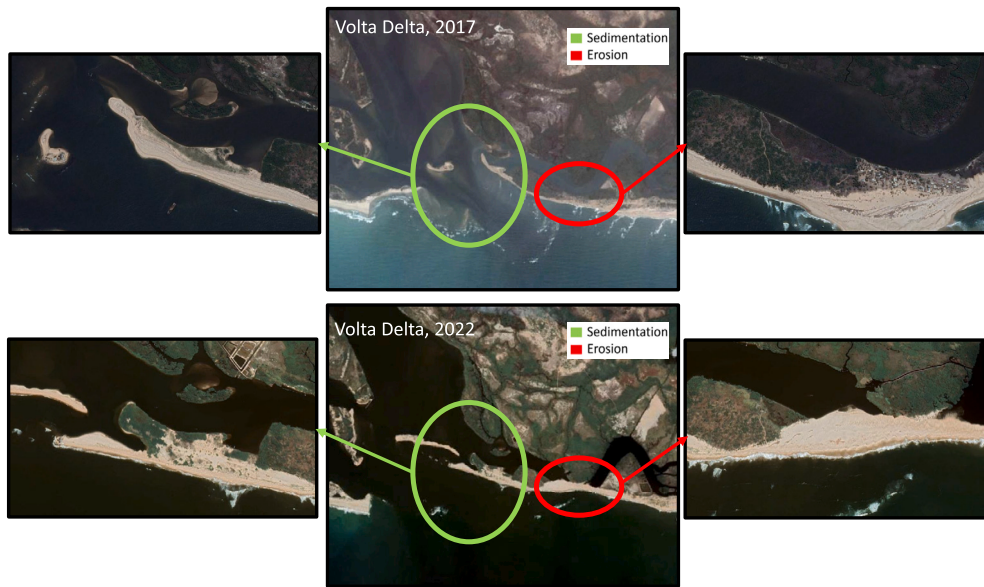
Fig. 4. Central panels: comparison between the Volta Delta in 2017 (top) and 2022 (bottom), highlighting two specific regions exhibiting erosion (marked by a red circle) and sedimentation (indicated by a green circle). The lateral panels provide a closer look at these chosen areas, with the left panels focusing on the sedimentation zone and the right panels on the erosion zone. Basemap: Google Earth.

3. Method: Sentinel-1 change detection thresholds

A 209-image stack in the area of interest is co-registered using GEE. All images are from the ascending orbit 74 (ASC74) between 2017/09/12 and 2021/03/13. The processing steps are illustrated in Fig. 3.

Let σ_0 be the radar reflectivity per unit area in ground range, and $\Delta\sigma_0$ its (temporal) variation. To estimate thresholds on $\Delta\sigma_0$, ascribable to erosion or sedimentation phenomena, a change detection technique is implemented. Change detection techniques for SAR data span various categories (Rignot and Van Zyl, 1993): in the first, changes are tracked through time based on stable features, with rectification for geometric distortions; the second category relies on temporal radar backscatter differences, demanding stable calibration and precise spatial registration; lastly, change detection techniques can involve data from multiple sensors. In this work, a $\Delta\sigma_0$ comparison between averaged multi-temporal images is conducted. Specifically, 17 images collected in the last months (September to December) of 2017 are averaged, and the same number of images is averaged in the last months of 2020 to evaluate thresholds of $\Delta\sigma_0$ for the same period of the year. Surface roughness, wind, precipitation, soil moisture, and tidal conditions are among the main drivers affecting SAR signal in coastal environments (Di Biase and Hanssen, 2021; Di Biase et al., 2022). Thanks to the high number of averaged images, the effect of these variables is reduced. Both VV and VH polarization are averaged.

Fig. 5 displays the σ_0 values in the multitemporal stack of 2017 and 2020 for VV (saturated in the interval $[-15, 10]$ dB) and VH (saturated in the interval $[-25, 5]$ dB) polarization, respectively. The images clearly show sedimentation and erosion areas, previously identified by comparing optical images, cf. Fig. 4.

To identify thresholds capable of detecting erosion and sedimentation phenomena over images normalized with respect to the satellite angle of view, the $\Delta\sigma_0$ of each pixel is evaluated for the 2017 and 2020 multi-temporally averaged stack, for both polarizations. The $\Delta\sigma_0$ values from the selected study areas (see Fig. 4) are utilized to determine threshold values for assessing erosion and sedimentation phenomena. This analysis also aids in identifying which polarization is more sensitive when employing the change detection methodology.

Table 1
Number of pixels per year within the erosion masks in the interested area.

| Polarization	2018	2019	2020
VH	1	152	177
VV	3	127	205

4. Results

In this section, we employ erosion and sedimentation thresholds to estimate areas affected by these two phenomena, respectively. The subsequent analysis of the results is complemented by hypotheses that aim to provide insights into the observed phenomena.
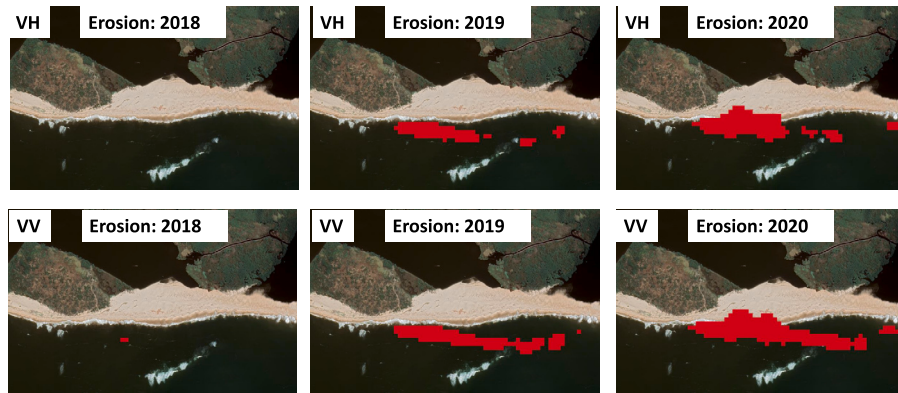
4.1. Erosion

To mitigate seasonal effects, we average σ_0 of Sentinel-1 acquisitions during the last trimester of each year from 2017 to the end of 2020. Establishing 2017 as the reference year, we evaluate $\Delta\sigma_0$ in VH and VV polarizations, identifying erosion events in 2018, 2019, and 2020 compared to 2017 (see Fig. 6). Erosion masks, employing VV polarization and a $\Delta\sigma_0 \leq -4$ dB threshold, exhibit more extensive coverage than VH polarization with $\Delta\sigma_0 \leq -8$ dB. Utilizing a more discerning VH threshold, i.e., $\Delta\sigma_0 \leq -9$ dB, proves successful in filtering out non-realistic offshore erosion areas. However, this more stringent threshold also results in a further reduction of the identified eroded area. Conversely, employing a less stringent threshold would lead to a substantial increase in the number of offshore pixels. This underscores the efficacy of VV polarization in change detection for identifying erosion areas. Subsequently, the assessment of erosion areas is presented in Fig. 7, showing the erosion mask in the area of interest obtained by comparing the averaged images of 2020 and 2017 (VV polarization). Background maps from Google Earth offer a visual representation of the evolution of erosion over time (top panel: before the study period; bottom panel: after the study period).

Fig. 6 also delineates that erosion phenomena initiate in 2019 and intensify throughout 2020. Table 1 provides details on the number of pixels in the erosion mask for the assessed years. In 2018, only three pixels for VV polarization (and one for VH) experience erosion, whereas by
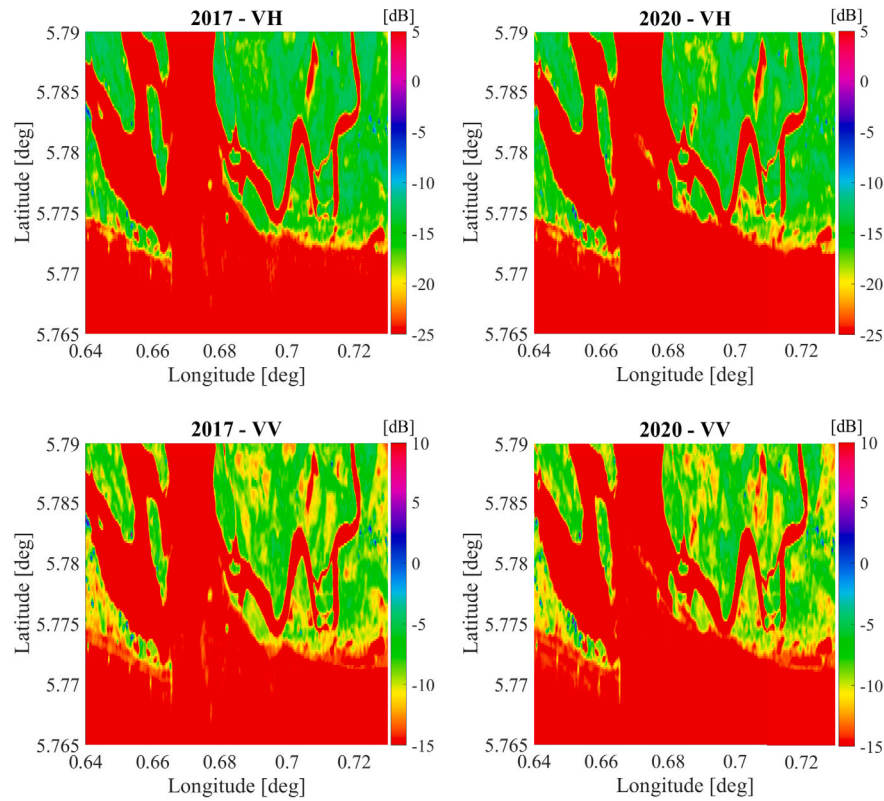
Fig. 5. Comparison between σ_0 values (indicated on the colorbar) in the multitemporal stack of 2017 and 2020. Top: VH polarization, saturated in the range $[-25, 5]$ dB. Bottom: VV polarization, saturated in the range $[-15, 10]$ dB.

Fig. 6. Erosion masks (red areas) in the years 2018 (left), 2019 (center) and 2020 (right) with respect to 2017. Top: VH polarization, with assumed erosion threshold value $\Delta\sigma_0 \leq -8$ dB. Bottom: VV polarization, with assumed erosion threshold value $\Delta\sigma_0 \leq -4$ dB. Basemap: Google Earth, 2023.

2020, the count of erosion pixels increases to 205 for VV polarization. Considering a pixel size of $20\,\text{m} \times 20\,\text{m}$, the area subjected to erosion between 2017 and 2020 amounts to 8.2 ha.

4.1.1. Temporal evolution analysis of erosion processes

To assess the temporal evolution of erosion phenomena, we conducted an analysis of the mean backscatter value on the erosion mask presented in Fig. 7, spanning from September 2017 to March 2021. For this analysis, the backscatter values were converted from decibels to linear, and to mitigate short-term effects like wind, tide level, and noise, a moving average over a two-month (8 images) interval was applied. The resulting trends are visualized in Fig. 8, where the blue line represents the average backscatter for VV polarization, decreasing from 0.11 to 0.03. In contrast, the red line, representing VH polarization, exhibits a decrease from 0.3 to a value ten times smaller. These trends align

with the findings in Table 1: in 2018, the backscatter variation - linked to the erosion rate - is not particularly pronounced. However, starting from 2019, especially in the latter part of the year, a significant decrease in backscatter becomes evident. This reinforces the observation of a notable acceleration in the erosion rate during that year. In the second half of 2019, the VV backscatter value is halved within a few months (decreasing from 0.08 to 0.04). Following this period, the reduction appears to slow down, suggesting a relatively stable situation until the end of the analyzed period. An additional hypothesis is proposed, suggesting that this stabilization may be attributed to complete water coverage over the considered erosion mask area.

In our analysis of the erosion mask, we delved into another aspect aiming to assess the effectiveness of the thresholds established in Sect. 3: the probability density of backscatter values. Figs. 9a and 9b show the probability density at six-month intervals for selected images
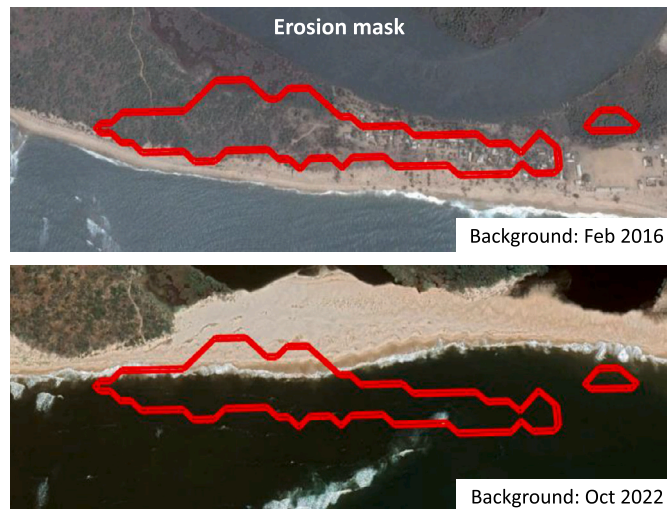
Fig. 7. Erosion mask (obtained by comparing the averaged image of 2020 and the one of 2017), VV polarization, represented by the red polygon. In the background maps (Google Earth) it is possible to notice the evolution of the erosion over time (top panel: before the study period; bottom panel: after the study period).

Fig. 8. Backscatter trend evaluated in the erosion mask, VH (red) and VV (blue) polarization.

Table 2
Number of pixels per year within the sedimentation masks in the interested area.

Polarization	2018	2019	2020
VH	0	78	128
VV	3	88	157

in VH and VV polarizations concerning erosion mask pixels. Fig. 9a underscores that, by the beginning of 2021, approximately 90% of the pixels exhibit a backscatter value at the peak (around -26 dB), with only about 10% displaying higher backscatter values. This observation strongly supports our hypothesis regarding the inundation of the study area. Furthermore, when examining the preceding years, characterized by a mixture of water and land, the probabilistic values fell within a range between -20 dB and -14 dB. Calculating the difference between the average σ_0 value in this range and the peak density value at the end of our investigation period for Fig. 9a, a $\Delta\sigma_0$ of about -8 dB is obtained, corresponding to the erosion threshold adopted for VH polarization. The figure associated with VV polarization (Fig. 9b) shows a similar trend. At the end of the investigation period, the density peak, at about -16 dB, has a value of approximately 60%. Considering the range of σ_0 values at the start of the period (between -12 dB and -8 dB), the difference between the lowest value of this range and the density peak at the beginning of 2021 is about -4 dB, assumed to be the VV threshold. During the period from September 2019 to February 2020, evident in VV polarization, the density peak shifts from -11 dB to -16 dB. Both figures affirm the earlier observation regarding the increasing rate of erosion phenomena starting from the second half of 2019.

4.2. Sedimentation

Following the methodology outlined in Sect. 4.1 and leveraging the thresholds presented in Sect. 3, we execute an examination of the sedimentation area illustrated in Fig. 4. The established sedimentation thresholds are $\Delta\sigma_0 \geq 4$ dB for VV polarization and $\Delta\sigma_0 \geq 8$ dB for VH polarization. By applying these criteria to the computed $\Delta\sigma_0$ concerning the reference year (2017), annual sedimentation masks are derived for each subsequent year, as shown in Fig. 10. The sedimentation mask, generated by contrasting the averaged image from 2020 with the averaged image of 2017 for VV polarization, is delineated in Fig. 11. In Fig. 11, the background map shows the evolution of sediments over time, both before the study period in the top panel and after in the bottom panel. The VH mask exhibits no pronounced deviation compared to the VV mask and remains devoid of false areas. The present analysis shows that the two polarizations manifest a parallel sensitivity to sedimentation phenomena. As presented in Table 2, the count of pixels encompassed in the mask for both VV and VH polarizations escalates considerably between 2018 and 2020. In this scenario, VV and VH
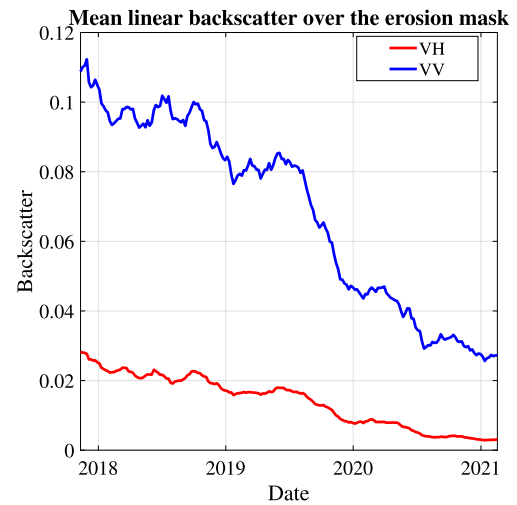
masks incorporate a comparable number of pixels, and no spurious sedimentation areas are identified with VH polarization, contrasting with the challenges observed in erosion area detection. Across the period from 2017 to 2020, an expanse of 6.2 ha undergoes sedimentation when considering a pixel size of 20 m × 20 m.

#### 4.2.1. Temporal evolution analysis of sedimentation processes

Fig. 12 illustrates the mean linear backscatter trend evaluated on the sedimentation mask from Fig. 10 as a function of time. At the start date, the mean values in the two polarizations are similar to the values evaluated in the erosion mask at the end of the considered period (see Fig. 8), characterized by pixels covered by water. From 2019, the mean backscatter value rapidly increases for both polarizations, with a sudden increment from the beginning of 2020. The maximum backscatter peak is reached in mid-2020, with a value of approximately 0.18 for VV and approximately 0.04 for VH. In the last 9 months of the considered period, the backscatter rapidly decreases, reaching a similar value compared to the erosion mask in 2017 (approximately 0.12 for VV and approximately 0.03 for VH).

Several hypotheses arise regarding the described phenomena. The first follows from the observation that sedimentation reaches its maximum peak in mid-2020 and decreases afterward. The small island, created by sedimentary deposits, reaches its maximum area in mid-2020; afterward, the water starts covering part of the sediments again, reducing the island's dimension. A second hypothesis, suggested by observing the backscatter values, is that the sedimentation area does not vary its dimension, but there is a change in its coverage: while sedimentation phenomena are still in progress, the presence of some coverage with high backscattering material increases. Subsequently, the coverage becomes similar to that of the erosion area at the start of 2017 (e.g., the presence of vegetation), and the backscatter values assume the characteristic values of the tropical coastal environment (0.12 for VV and 0.03 for VH). A third hypothesis is that both the area and coverage change over the considered period: the ocean and the river erode part of the island, and at the same time, the coverage of the sedimentary deposits
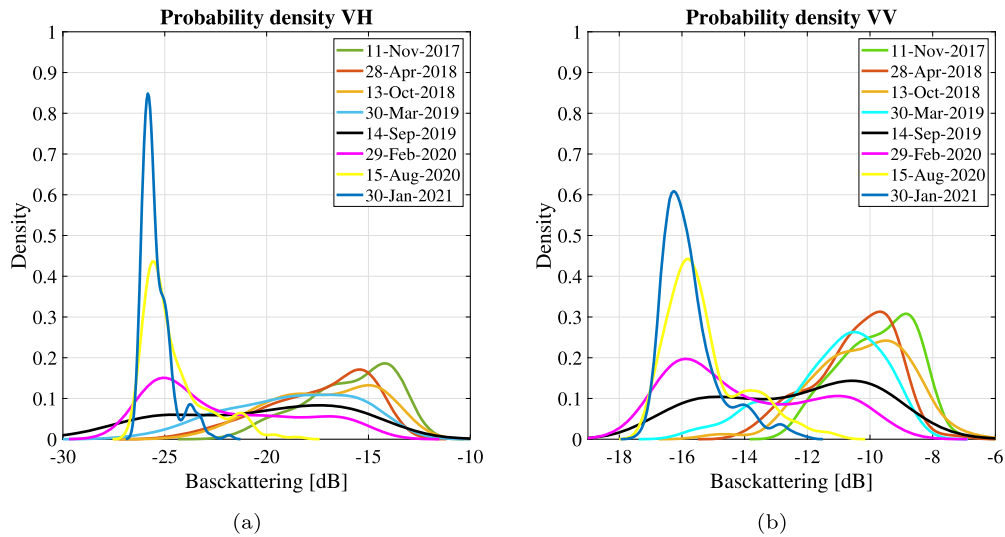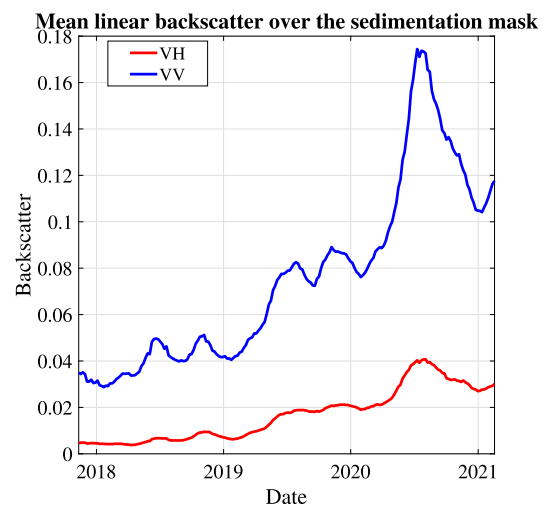
Fig. 9. Probability density within the erosion mask for selected images taken every 6 months: (a) VH polarization; (b) VV polarization. Data processed with two-months moving average centered on the indicated date.
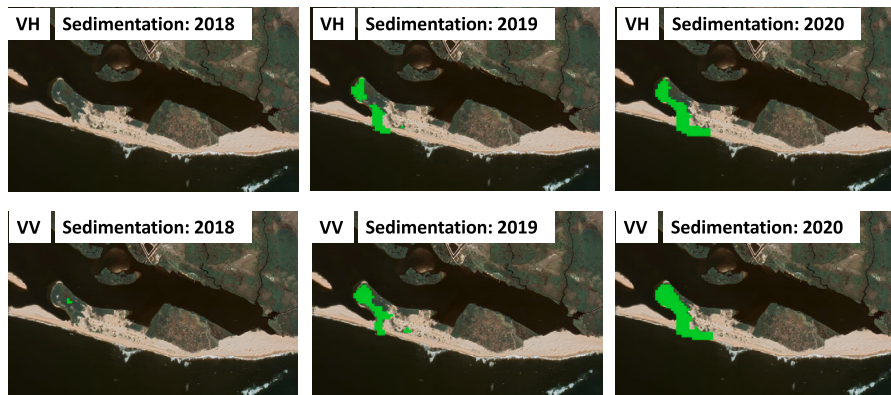
Fig. 10. Sedimentation masks (green areas) in the years 2018 (left), 2019 (center) and 2020 (right) with respect to 2017. Top row: VH polarization, with the assumed erosion threshold value $\Delta\sigma_0 \leq -8$ dB. Bottom row: VV polarization. The assumed erosion threshold value is $\Delta\sigma_0 \leq -4$ dB. Basemap: Google Earth, 2023.

Fig. 11. Sedimentation mask (obtained by comparing the averaged image of 2020 and the one of 2017), VV polarization, represented by the green polygon. In the background maps (Google Earth) it is possible to notice the evolution of the sediments over time (top panel: before the study period; bottom panel: after the study period).

Fig. 12. Backscatter trend on the sedimentaion mask, VH (red) and VV polarization (blue).

changes (e.g., vegetation starts growing after the situation becomes more stable). These phenomena become more apparent when analyz-
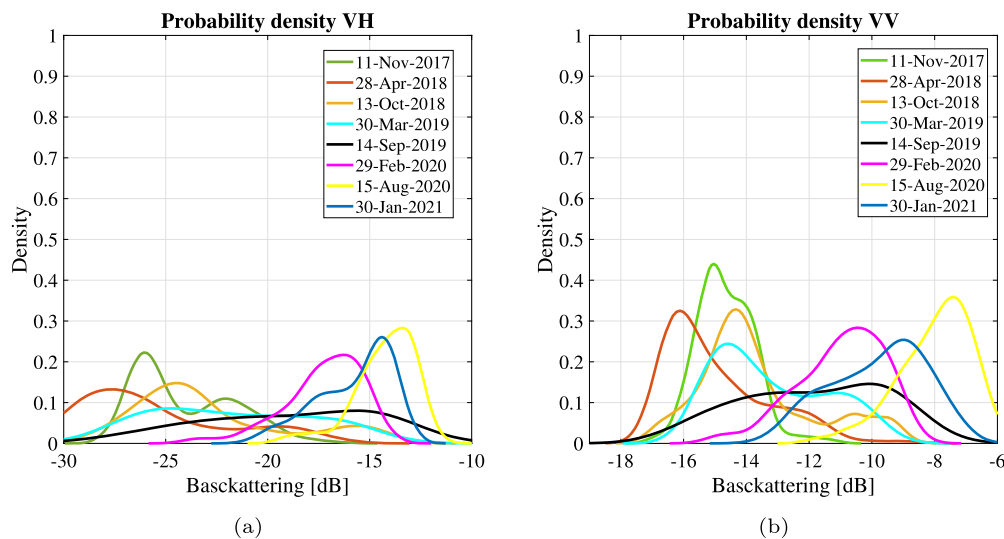
Fig. 13. Probability density within the sedimentation mask for selected images taken every 6 months: (a) VH polarization; (b) VV polarization. Data processed with two-months moving average centered on the indicated date.

ing the probability density over six-month intervals, as previously done for erosion. Fig. 13a displays the probability density of different images in VH polarization. It can be observed that: a) the distribution curves shift to the right, corresponding to higher backscatter values (measured in dB); b) the right-most curve is not the last one but the one referred to August 2020; afterward, as commented in Fig. 12, the last curve shifts to the left. Similar to erosion, the sedimentation thresholds considered in Sect. 3 can be confirmed by observing this graphic, where the characteristic value for the density peak at the highest sedimentation (close to -13 dB) is about 8 dB higher than the minimum range value characteristic of the area before the beginning of the process (between -28 dB and -21 dB).

Similar considerations hold for VV polarization (Fig. 13b), where the density peak of the highest sedimentation curve (yellow curve) is -7 dB, and the initial range before the sedimentation process is between -17 dB and -12 dB. This confirms the efficacy of the adopted threshold ($\Delta\sigma_0 \geq 4$ dB).

The figure referring to VV polarization presents two further interesting aspects. The range of the initial and ending curves is rather narrow, i.e., the tops of the green and yellow curves are distinct and do not overlap. This clear distinction facilitates the reduction of false detection areas. A second aspect is that the last curve (blue), presenting a density peak and in general shifted to the left with respect to the curve of maximum sedimentation (yellow), slightly overlaps the curves of the first stage of the phenomena; moreover, it presents a larger bell compared to the curve of highest sedimentation. The hypothesis is that only part of the pixels previously affected by sedimentation is now affected by erosion, and a change of coverage occurs.

5. Conclusion and recommendations

Sentinel-1 images have been exploited for determining erosion and sedimentation phenomena in the Keta lagoon (Ghana) using a change detection methodology. Change detection, estimated for both VV and VH polarizations over a four-year interval, involved evaluating erosion and sedimentation thresholds (± 4 dB for VV, ± 8 dB for VH). VV polarization demonstrated superior results for erosion detection, a conclusion supported by a comparison with optical images from Google Earth, underscoring the efficacy of the method. By analyzing the probability density of backscatter values at pixel locations associated with sedimentation or erosion, along with annual comparisons, the study facilitated the quantification of the affected areas: 8.2 ha for erosion and 6.2 ha for sedimentation over the considered years.

Building on these insights, future studies in erosion and sedimentation dynamics along coastal regions should leverage the presented methodology. This entails exploring diverse scenarios and conducting comparative analyses with different sensors to refine the approach, optimizing selections based on specific coastal characteristics. To enhance the comprehensiveness of these studies, integrating data on anthropogenic factors, such as construction, urbanization, and agricultural practices, is crucial. Extending temporal studies to longer periods can uncover nuanced trends in erosion and sedimentation dynamics, providing valuable insights into the evolution of coastal processes. Additionally, the integration of data from multiple sensors, including optical imagery, holds promise for enhancing the accuracy and reliability of assessments, offering a more comprehensive view of coastal dynamics.

Declaration of competing interest

The authors declare that they have no known competing financial interests of personal relationships that could have appeared to influence the work reported in this paper.

References

Addo, K.A., Jayson-Quashigah, P.-N., Codjoe, S.N.A., Martey, F., 2018. Drone as a tool for coastal flood monitoring in the Volta Delta, Ghana. Geoenviron. Disasters 5, 1–13.

Alves, B., Angnuureng, D.B., Morand, P., Almar, R., 2020. A review on coastal erosion and flooding risks and best management practices in West Africa: what has been done and should be done. J. Coast. Conserv. 24, 1–22.

Angnuureng, B., Appearing Addo, K., Wiafe, G., 2013. Impact of sea defense structures on downdrift coasts: the case of Keta in Ghana. Acad. J. Environ. Sci. 1, 104–121.

Angnuureng, D.B., Jayson-Quashigah, P.-N., Almar, R., Stieglitz, T.C., Anthony, E.J., Aheto, D.W., Appearing Addo, K., 2020. Application of shore-based video and unmanned aerial vehicles (drones): complementary tools for beach studies. Remote Sens. 12, 394.

Ankrah, J., Monteiro, A., Madureira, H., 2023. Shoreline change and coastal erosion in West Africa: a systematic review of research progress and policy recommendation. Geosciences 13, 59.

Apostolopoulos, D., Nikolakopoulos, K., 2021. A review and meta-analysis of remote sensing data, GIS methods, materials and indices used for monitoring the coastline evolution over the last twenty years. Eur. J. Remote Sens. 54, 240–265.

Appearing Addo, K., Brempong, E., Jayson-Quashigah, P., 2020. Assessment of the dynamics of the Volta river estuary shorelines in Ghana. Geoenviron. Disasters 7, 1–11.

Armah, A., 1991. Coastal erosion in Ghana: causes, patterns, research needs and possible solutions. In: Coastal Zone'91. ASCE, pp. 2463–2473.

Armah, A., Amlalo, D., 1998. Coastal zone profile of Ghana. Ministry of Environment, Science and Technology.

Baghdadi, N., Gaultier, S., King, C., 2002. Retrieving surface roughness and soil moisture from synthetic aperture radar (SAR) data using neural networks. Can. J. Remote Sens. 28, 701–711.

Boardman, J., 2016. The value of Google Earth™ for erosion mapping. Catena 143, 123–127.

Boardman, J., Favis-Mortlock, D., Foster, I., 2015. A 13-year record of erosion on badland sites in the Karoo, South Africa. Earth Surf. Process. Landf. 40, 1964–1981.

Boateng, I., 2012. An application of GIS and coastal geomorphology for large scale assessment of coastal erosion and management: a case study of Ghana. J. Coast. Conserv. 16, 383–397.

Borrelli, L., Cofone, G., Coscarelli, R., Gullà, G., 2015. Shallow landslides triggered by consecutive rainfall events at Catanzaro strait (Calabria–Southern Italy). J. Maps 11, 730–744.

Bovolo, F., Bruzzone, L., 2007. A split-based approach to unsupervised change detection in large-size multitemporal images: application to tsunami-damage assessment. IEEE Trans. Geosci. Remote Sens. 45, 1658–1670.

Boye, C.B., Fiadonu, E.B., 2020. Lithological effects on rocky coastline stability. Heliyon 6.

Brempong, E.K., Angnuureng, D.B., Appeaning Addo, K., Jayson-Quashigah, P.-N., 2021. Short-term seasonal changes of the Dzita beach of Ghana using geographic information system and photogrammetry. Interpretation 9, SH87–SH97.

Choi, M., Hur, Y., 2012. A microwave-optical/infrared disaggregation for improving spatial representation of soil moisture using AMSR-E and MODIS products. Remote Sens. Environ. 124, 259–269.

Di Biase, V., Hanssen, R.F., 2021. Environmental strain on beach environments retrieved and monitored by spaceborne synthetic aperture radar. Remote Sens. 13, 4208.

Di Biase, V., Kuschnerus, M., Lindenbergh, R.C., 2022. Permanent laser scanner and synthetic aperture radar data: correlation characterisation at a sandy beach. Sensors 22, 2311.

Dong, Z., Wang, Z., Liu, D., Song, K., Li, L., Jia, M., Ding, Z., 2014. Mapping wetland areas using Landsat-derived NDVI and LSWI: a case study of West Songnen Plain, Northeast China. J. Indian Soc. Remote Sens. 42, 569–576.

Elhag, M., Bahrawi, J.A., 2017. Soil salinity mapping and hydrological drought indices assessment in arid environments based on remote sensing techniques. Geosci. Instrum. Method. Data Syst. 6, 149–158.

Elhag, M., Psilovikos, A., Manakos, I., Perakis, K., 2011. Application of the sebs water balance model in estimating daily evapotranspiration and evaporative fraction from remote sensing data over the Nile delta. Water Resour. Manag. 25, 2731–2742.

French, J., Burningham, H., 2009. Coastal geomorphology: trends and challenges. Prog. Phys. Geogr. 33, 117–129.

Gens, R., 2010. Remote sensing of coastlines: detection, extraction and monitoring. Int. J. Remote Sens. 31, 1819–1836.

Goodman, J.W., 1976. Some fundamental properties of speckle. J. Opt. Soc. Am. 66, 1145–1150.

Gulácsi, A., Kovács, F., 2020. Sentinel-1-imagery-based high-resolution water cover detection on wetlands, aided by Google Earth engine. Remote Sens. 12, 1614.

Hachemi, K., Grecu, F., Ioana-Toroimac, G., Constantin, D.M., Ozer, A., 2020. The diachronic analysis of island dynamics along the Vedea-Olteniţa Danube river sector using SAR imagery. Mediterr. Geosci. Rev., 1–15.

Hachemi, K., Thomas, Y., Senhoury, A., Martin, T., 2015. Multitemporal analysis of the city of Nouakchott (Mauritania) based on ASAR images. Geoinf. Geostat. 3, 1–7.

Hackney, C., Carling, P., 2011. The occurrence of obtuse junction angles and changes in channel width below tributaries along the Mekong River, South-East Asia. Earth Surf. Process. Landf. 36, 1563–1576.

Horritt, M., Mason, D., Luckman, A., 2001. Flood boundary delineation from synthetic aperture radar imagery using a statistical active contour model. Int. J. Remote Sens. 22, 2489–2507.

Jayson-Quashigah, P.-N., Addo, K.A., Amisigo, B., Wiafe, G., 2019. Assessment of short-term beach sediment change in the Volta Delta coast in Ghana using data from Unmanned Aerial Vehicles (Drone). Ocean Coast. Manag. 182, 104952.

Kana, T.W., 2003. Coastal Erosion and Solutions: A Primer. Coastal Science & Engineering LLC.

Lamptey, P.N., Doe, C.E., Addi, M., Botchway, C.G., 2022. Assessing the feasibility of Landsat satellite data in monitoring water body and shoreline change along the coast of Keta. J. Coast. Conserv. 26, 50.

Lee, J.-S., 1980. Digital image enhancement and noise filtering by use of local statistics. IEEE Trans. Pattern Anal. Mach. Intell., 165–168.

Lee, J.-S., 1981. Refined filtering of image noise using local statistics. Comput. Graph. Image Process. 15, 380–389.

Lee, J.-S., 1986. Speckle suppression and analysis for synthetic aperture radar images. Opt. Eng. 25, 255636.

Ly, C.K., 1980. The role of the Akosombo Dam on the Volta river in causing coastal erosion in central and eastern Ghana (West Africa). Mar. Geol. 37, 323–332.

Martinis, S., Twele, A., 2010. A hierarchical spatio-temporal Markov model for improved flood mapping using multi-temporal X-band SAR data. Remote Sens. 2, 2240–2258.

Natesan, U., Parthasarathy, A., Vishnunath, R., Kumar, G.E.J., Ferrer, V.A., 2015. Monitoring longterm shoreline changes along Tamil Nadu, India using geospatial techniques. Aquat. Proc. 4, 325–332.

Ngo, K.D., Lechner, A.M., Vu, T.T., 2020. Land cover mapping of the Mekong Delta to support natural resource management with multi-temporal sentinel-1a synthetic aperture radar imagery. Remote Sens. Appl., Soc. Environ. 17, 100272.

Nikolakopoulos, K., Kyriou, A., Koukouvelas, I., Zygouri, V., Apostolopoulos, D., 2019. Combination of aerial, satellite, and UAV photogrammetry for mapping the diachronic coastline evolution: the case of Lefkada island. ISPRS Int.l J. Geo-Inf. 8, 489.

Pandey, A.C., Kaushik, K., Parida, B.R., 2022. Google Earth engine for large-scale flood mapping using SAR data and impact assessment on agriculture and population of Ganga-Brahmaputra basin. Sustainability 14, 4210.

Pelich, R., Chini, M., Hostache, R., Matgen, P., López-Martínez, C., 2020. Coastline detection based on sentinel-1 time series for ship- and flood-monitoring applications. IEEE Geosci. Remote Sens. Lett. 18, 1771–1775.

Pethick, J.S., 1984. An introduction to coastal geomorphology. Technical Report. Dept. of Geography, Univ. of Hull.

Pilkey, O.H., Cooper, J.A.G., Lewis, D.A., 2009. Global distribution and geomorphology of fetch-limited barrier islands. J. Coast. Res. 25, 819–837.

Puplampu, D.A., Iddris, K., Alorbu, V., Asante, J.O., Takaman, J.L., Owusu, A.B., 2023. Shoreline change analysis of the eastern coast of Ghana between 1991 and 2020. J. Environ. Geogr. 16, 11–21.

Quegan, S., Le Toan, T., Yu, J.J., Ribbes, F., Floury, N., 2000. Multitemporal ERS SAR analysis applied to forest mapping. IEEE Trans. Geosci. Remote Sens. 38, 741–753.

Rahman, M.R., Shi, Z., Chongfa, C., 2009. Soil erosion hazard evaluation—an integrated use of remote sensing, GIS and statistical approaches with biophysical parameters towards management strategies. Ecol. Model. 220, 1724–1734.

Rignot, E.J., Van Zyl, J.J., 1993. Change detection techniques for ERS-1 SAR data. IEEE Trans. Geosci. Remote Sens. 33, 896–906.

Schoepfer, E., Spröhnle, K., Kranz, O., Blaes, X., Kolomaznik, J., Hilgert, F., Bartalos, T., Kemper, T., 2017. Towards a multi-scale approach for an Earth observation-based assessment of natural resource exploitation in conflict regions. Geocarto Int. 32, 1139–1158.

Sepuru, T.K., Dube, T., 2018. An appraisal on the progress of remote sensing applications in soil erosion mapping and monitoring. Remote Sens. Appl., Soc. Environ. 9, 1–9.

Sharma, L.K., Gupta, R., Pandey, P.C., 2021. Future aspects and potential of the remote sensing technology to meet the natural resource needs. In: Advances in Remote Sensing for Natural Resource Monitoring, pp. 445–464.

Ulaby, F., Moore, R., Fung, A., 1982. Microwave Remote Sensing: Active and Passive. Volume 2-Radar Remote Sensing and Surface Scattering and Emission Theory. Artech House, Norwood.

Vandebroek, E., Lindenbergh, R., Van Leijen, F., De Schipper, M., De Vries, S., Hanssen, R., 2017. Semi-automated monitoring of a mega-scale beach nourishment using high-resolution TerraSAR-X satellite data. Remote Sens. 9, 653.

Vrieling, A., 2006. Satellite remote sensing for water erosion assessment: a review. Catena 65, 2–18.

Wang, Y., Allen, T.R., 2008. Estuarine shoreline change detection using Japanese ALOS palsar HH and JERS-1 L-HH SAR data in the Albemarle-Pamlico Sounds, North Carolina, USA. Int. J. Remote Sens. 29, 4429–4442.

Wellens-Mensah, J., Armah, A., Amlalo, D., Tetteh, K., 2002. Development and protection of the coastal and marine environment in sub-Saharan Africa, Ghana. Nat. Rep. Phase 1.

Zhu, Q., Li, P., Li, Z., Pu, S., Wu, X., Bi, N., Wang, H., 2021. Spatiotemporal changes of coastline over the Yellow River Delta in the previous 40 years with optical and SAR remote sensing. Remote Sens. 13, 1940.

Zribi, M., Taconet, O., Le Hégarat-Mascle, S., Vidal-Madjar, D., Emblanch, C., Loumagne, C., Normand, M., 1997. Backscattering behavior and simulation comparison over bare soils using SIR-C/X-SAR and ERASME 1994 data over Orgeval. Remote Sens. Environ. 59, 256–266.